

Quantitative Diagnosis of Malignant Pleural Effusions by Single-Cell Mechanophenotyping

Henry T. K. Tse,^{1,2,3} Daniel R. Gossett,^{1,2,3} Yo Sup Moon,⁴ Mahdokht Masaeli,¹ Marie Sohsman,⁵ Yong Ying,⁵ Kimberly Mislick,⁵ Ryan P. Adams,⁶ Jianyu Rao,^{3,5,7*} Dino Di Carlo^{1,3,7*}

Biophysical characteristics of cells are attractive as potential diagnostic markers for cancer. Transformation of cell state or phenotype and the accompanying epigenetic, nuclear, and cytoplasmic modifications lead to measurable changes in cellular architecture. We recently introduced a technique called deformability cytometry (DC) that enables rapid mechanophenotyping of single cells in suspension at rates of 1000 cells/s—a throughput that is comparable to traditional flow cytometry. We applied this technique to diagnose malignant pleural effusions, in which disseminated tumor cells can be difficult to accurately identify by traditional cytology. An algorithmic diagnostic scoring system was developed on the basis of quantitative features of two-dimensional distributions of single-cell mechanophenotypes from 119 samples. The DC scoring system classified 63% of the samples into two high-confidence regimes with 100% positive predictive value or 100% negative predictive value, and achieved an area under the curve of 0.86. This performance is suitable for a prescreening role to focus cytopathologist analysis time on a smaller fraction of difficult samples. Diagnosis of samples that present a challenge to cytology was also improved. Samples labeled as “atypical cells,” which require additional time and follow-up, were classified in high-confidence regimes in 8 of 15 cases. Further, 10 of 17 cytology-negative samples corresponding to patients with concurrent cancer were correctly classified as malignant or negative, in agreement with 6-month outcomes. This study lays the groundwork for broader validation of label-free quantitative biophysical markers for clinical diagnoses of cancer and inflammation, which could help to reduce laboratory workload and improve clinical decision-making.

INTRODUCTION

Pleural effusions are valuable sources of diagnostic information. In a healthy individual, the volume of pleural fluid—an acellular liquid—is between 7 and 16 ml; however, systemic imbalances and disease may lead to an abnormal accumulation of fluid containing disseminated cells (up to 2 liters) (1, 2). Hence, pleural fluid samples can provide insight into patient health, such as the status of infections, inflammatory processes, and malignant diseases.

The examination of pleural effusions for malignancies in clinical settings relies on cytological analysis as the gold standard. The cytopathologist examines cells from cell smears and cell blocks and identifies features of cytoplasmic and nuclear morphology suggestive of malignancy, including high nuclear-to-cytoplasmic ratios, hypochromatic cytoplasm, and dense, dark nuclei. Categories of diagnoses include negative for malignant cells (NMC), acute inflammation (AI), chronic/mixed inflammation (CMI), atypical cells (ACs; equivocal for malignancy), and malignant pleural effusions (MPEs). Determination of disease pathology requires manual expert screening and confirmation where the level of scrutiny depends on the complexity of the sample. “Biological noise,” arising from the similar morphology of malignant

cells and reactive mesothelial (RM) cells (cells derived from the mesothelium membrane) or a high density of leukocyte populations, can mask possible epithelial or hematopoietic malignancies (3, 4). Hence, the sensitivity for diagnosis of MPEs spans a wide range between 40 and 90%, depending on several factors including the source of the malignancy and experience of the cytopathologist (5–8).

Conclusive diagnosis of pleural effusions often requires follow-up molecular label-assisted techniques, such as analysis of immuno-histochemical or biochemical markers characteristic of disease phenotype using flow cytometry and immunohistochemistry. However, even with these drawbacks, cytological analysis of pleural fluids is important considering the clinical value of the findings, in which a positive finding of malignancy usually indicates late-stage disease processes and calls for aggressive treatment. Conventional preparation of pleural effusions for cytological analysis involves numerous processing steps, staining reagents, and prescreening reads by cytotechnologists before the cytopathologist reading. Although many of these protocols are now automated, sample preparation can take on the order of 1 to 2 hours in batch and still requires some manual processes. Because most of the pleural effusion samples are identified as negative for malignancies (>80%), it is an inefficient and costly process to prepare and analyze every sample at the same level of detail. Thus, a simple, quick, and automated prescreening tool to identify high-risk patients would maximize the use of available resources, reduce sample processing burdens, reduce chances of cross-contamination, and decrease the time to diagnosis.

An approach that reduces labor and costs associated with labeling and sample preparation would be ideal to achieve this. Label-free biomarkers, including the mechanical properties of single cells, or “mechanophenotype,” have shown promise in clinical diagnostics

¹Department of Bioengineering, University of California, Los Angeles, Los Angeles, CA 90095, USA. ²CytoVale Inc., South San Francisco, CA 94080, USA. ³California NanoSystems Institute, University of California, Los Angeles, Los Angeles, CA 90095, USA. ⁴Harvard College, Harvard University, Cambridge, MA 02138, USA. ⁵Department of Pathology and Laboratory Medicine, University of California, Los Angeles, Los Angeles, CA 90095, USA. ⁶School of Engineering and Applied Sciences, Harvard University, Cambridge, MA 02138, USA. ⁷Jonsson Comprehensive Cancer Center, Los Angeles, CA 90095, USA.

*Corresponding author. E-mail: dicarlo@seas.ucla.edu (D.D.C.); jrao@mednet.ucla.edu (J.R.)

(6). For example, the mechanical properties of cancer cell lines differ from their benign counterparts in culture. Although it has long been known that tumors are stiffer than neighboring healthy tissue (7, 8), individual cancer cells are typically softer, and this deformability (that is, the ability to change shape under an applied load) may confer their ability to migrate through tissue. Several methods have been developed or adapted to probe mechanical properties of cells, including atomic force microscopy (AFM) (7, 9, 10), micropipette aspiration (11, 12), cell transit analysis (13–18), microfluidic optical stretching (8, 19), and hydrodynamic forces (20, 21). Yet, previous technology was limited to interrogating a few cells in small clinical studies owing to the technological complexity. For example, AFM analysis of malignant cells isolated from pleural fluids demonstrated that these subpopulations are mechanically softer than the native cells (7), but the technological complexity requiring user intervention to preselect morphologically malignant cells limited the system throughput. Nevertheless, this initial work provided evidence that biophysical properties may be useful as a diagnostic marker.

Here, we evaluated the use of a technique for high-throughput single-cell mechanical analysis, previously developed by our group, called deformability cytometry (DC) (21), for diagnosing MPEs (Fig. 1). Because this technique screens cells at throughputs comparable to flow cytometry, we could quantify the biophysical characteristics of the cell population. In this study of 119 patients with pleural effusions of benign or malignant origin, we obtained more than 3000 single-cell biophysical measurements in each specimen assayed. This provided confidence in sampling heterogeneous populations and in establishing common outcome profiles. As a complementary method to slide-based cytology and follow-up techniques, DC has the capability to increase diagnostic accuracy and decrease healthcare costs.

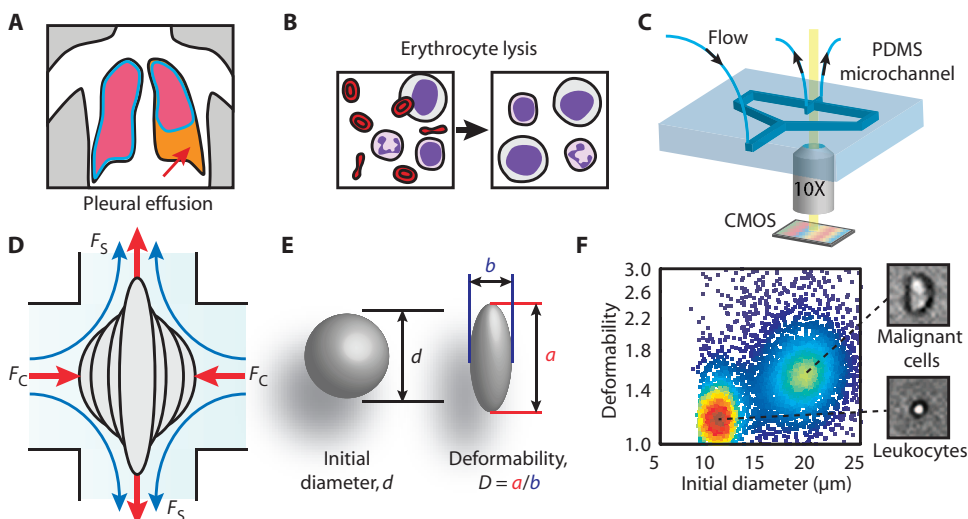


Fig. 1. DC: Mechanical phenotyping of pleural effusions. (A) Pleural effusions are drained from the pleural cavity around the lungs. (B) Erythrocytes are lysed off-chip to isolate nucleated cells before assay. (C) Cells are introduced into the polydimethylsiloxane (PDMS) microfluidic channel and then positioned and stretched under continuous flow. Stretching cells are imaged by a high-speed complementary metal-oxide semiconductor (CMOS) camera. (D) Cells are subjected to compressive (F_c) and shear (F_s) forces in the microchannel. (E) Initial diameter (d) and maximum aspect ratio (D) of the cell upon deformation are extracted from the sequences of images. (F) An example 2D biophysical profile plot of an MPE reveals two cell populations using diameter and deformability metrics.

RESULTS

Biophysical profile of negative for malignancy specimens

For this proof-of-concept clinical study, we applied DC (21) for diagnosing MPEs (Fig. 1). Briefly, a cell population obtained from the pleural cavity around the lungs and devoid of erythrocytes was accelerated through microfluidic channels and then rapidly decelerated by an opposing wall of fluid, experiencing hydrodynamic forces (Fig. 1, A to D). Quantitative metrics of cell deformability [D = maximum ratio of major (a) over minor (b) axis of the deforming cell] and initial size (d , diameter) were extracted from high-speed videos (Fig. 1E). By grouping biophysical profiles according to cytological diagnosis and validating these groups with separate data sets, we found unique profiles indicative of negative and malignant diagnoses. In samples diagnosed as NMC—without confounding inflammatory processes—the cellular composition was predominantly composed of nonactivated immune cells and benign mesothelial cells. Comparative analysis of these samples by DC revealed that the major feature of the NMC profile was a high-density population with small size ($d = 8$ to $12 \mu\text{m}$), rigid deformability ($D < 1.4$), and a limited variability in both size and deformability [$\{\text{median } d = 10.3 \mu\text{m}; \text{quartile 1 (Q1): } 9.2, \text{Q3: } 11.5\}$, (median $D = 1.32$; Q1: 1.15, Q3: 1.41)].

The quantitative biophysical metrics enabled grading based on common two-dimensional (2D) profile features associated with known clinical outcomes of NMC, AI, or CMI (Fig. 1F and fig. S1). Each sample's profile score was calculated using threshold-based decision classifiers to maximize accuracy of detecting malignancy, where the decision classifiers were trained on subsets of training data. The scores for each sample correlated with the probability of malignancy in rank order (1 to 10), where the higher the score, the increased likelihood of malignant disease. Characteristic DC profiles of NMC patients 1 to 4 are shown in Fig. 2 (scores were typically 1 or 2). The biophysical properties of this population closely resembled those measured when evaluating healthy leukocytes from peripheral blood (21).

Notably, in samples that were determined by cytology to contain an abundance of mesothelial cells, a defining feature was a distinct population of larger and stiffer cells. For example, in NMC patients 4 and 8 (Fig. 2), the DC profile showed a substantial population of cells with a diameter ranging from 15 to $20 \mu\text{m}$ and a deformability of < 1.4 . This feature appeared commonly in specimens with the RM cytology outcome—an outcome that is clinically important to distinguish from adenocarcinoma or malignant mesothelioma.

Biophysical profile of specimens with increased leukocyte activation

Samples negative for malignancy, but also associated with inflammatory processes, categorized as AI and CMI by cytology, had profiles distinct from each other as well as from NMC samples. Using our

DC approach, AI cases resulted in distinct profiles that consisted of a smaller-sized cell (8 to 12 μm) population with a subpopulation of highly deformable cells. The proportion of cells with $D > 1.4$ in AI cases was 16.6%, which was higher than that of NMC outcomes (1.4%). The median deformability of AI specimens was 1.56 and ranged from 1.45 to 1.67 ($n = 37$ patients). Representative DC profiles of AI patients 5 to 7 are shown in Fig. 2. This transformation, from rigid, resting leukocytes to a more deformable, activated state, agrees with what has been observed with this technique in vitro for neutrophil activation by *N*-formyl-Met-Leu-Phe (21).

CMI cases had a slightly larger size than AI (8 to 15 μm) and a larger distribution of D (1.0 to 3.0) around a median of 2.0. Pooling all CMI samples ($n = 33$), the proportion of cells with $D > 1.4$ was 24.7%. This represented an 18- and 1.5-fold increase in deformable cells compared to NMC and AI samples, respectively. Characteristic DC profiles of CMI patients 8 to 10 are shown in Fig. 2. In vitro activation of peripheral blood mononuclear cells by phytohemagglutinin has shown a similar biophysical response in our measurement system as for CMI cases (21).

Biophysical profile features unique to MPEs

Samples obtained from patients with MPEs typically contained a subpopulation of cells residing in the upper right DC quadrant: large (>17 μm) and highly deformable ($D > 1.4$) (Fig. 2, patients 11 to 20). MPE cases had more varied size and deformability cell clusters from patient to patient when compared to NMC, AI, and CMI cases, presumably owing to the wide range of origins of malignancy that accumulate in pleural fluids. The 29 MPE cases included breast adenocarcinoma ($n = 4$), ovarian adenocarcinoma ($n = 3$), mesothelioma ($n = 2$), soft tissue sarcoma ($n = 1$), pancreatic adenocarcinoma ($n = 1$), non-small cell lung carcinoma ($n = 1$), gastrointestinal carcinoma ($n = 7$), lymphoma ($n = 1$), leukemia ($n = 4$), prostate adenocarcinoma ($n = 1$), and cancers of unknown primary origin ($n = 4$). In most of these cases, DC profiles indicated features of AI or CMI concurrently with an increased percentage of large and deformable cells reflecting MPE (Fig. 2). Seldom noted in cytology diagnoses, these data may be able to provide valuable additional information regarding a patient's physiological state.

Pt. #	Clinical outcome	DC analysis		Pt. #	Clinical outcome	DC analysis	
		Def.	Size			Score	Def.
1	NMC			1	MPE, CMI		7
2	NMC			12	MPE, AI		7
3	NMC			13	MPE, CMI		8
4	NMC, RM			14	MPE		8
5	NMC, AI			15	MPE, AI		9
6	NMC, AI			16	MPE		9
7	NMC, AI			17	MPE		10
8	NMC, CMI, RM			18	MPE, CMI		10
9	NMC, CMI			19	MPE		10
10	NMC, CMI			20	MPE		10

Fig. 2. Example cases of NMC, AI, CMI, and MPEs. Samples from patients 1 to 10 exhibited characteristics representing NMC outcomes. In a subset of patients (samples 5 to 7), AI was indicated, whereas for patients 8 to 10, CMI was noted. Patients 11 to 20 represented samples collected from MPE; some MPE cases also had populations of cells reflecting AI and CMI. RM indicates that RM cells were present. The algorithm-based DC score (from 1 to 10) assigned a level of suspicion to each sample, where the higher the number, the increased likelihood of malignant cells.

Algorithmic scoring using characteristic profile features

We next developed a quantitative classification system that provided a score for each sample representing the likelihood of malignant disease, using DC profile features associated with negative and malignant pleural fluids (fig. S1). We pooled DC profiles from each clinically negative outcome (10 each from NMC, AI, and CMI) to create a generalized negative profile (Fig. 3A). We then defined 11 profile features, including the percentage of cells within the large (>17 μm) and deformable ($D > 1.4$) quadrant and the root mean square error (RMSE), describing deviation from fits of AI or CMI pooled data sets (see all 11 features in Table 1). A detailed description of the creation of these profile features can be found in Materials and Methods. We iteratively determined thresholds and weights for the 11 profile features that best classified the 119 patient samples. The thresholds and weights were, in turn, used to score each sample from 1 to 10 (1: least likely to be malignant, 10: most likely to be malignant). The distribution of scores for 119 samples (Fig. 3B) showed regions of high positive predictive value (PPV) of 100% for scores in the 9 and 10 range and high negative predictive value (NPV) of 100% for scores in the 1 to 6 range. In all, these high-confidence regions covered 63.0% of patient samples ($n = 75$). The remaining patient samples had equivocal profile scores of 7 and 8, where confounding factors were present such as profiles with

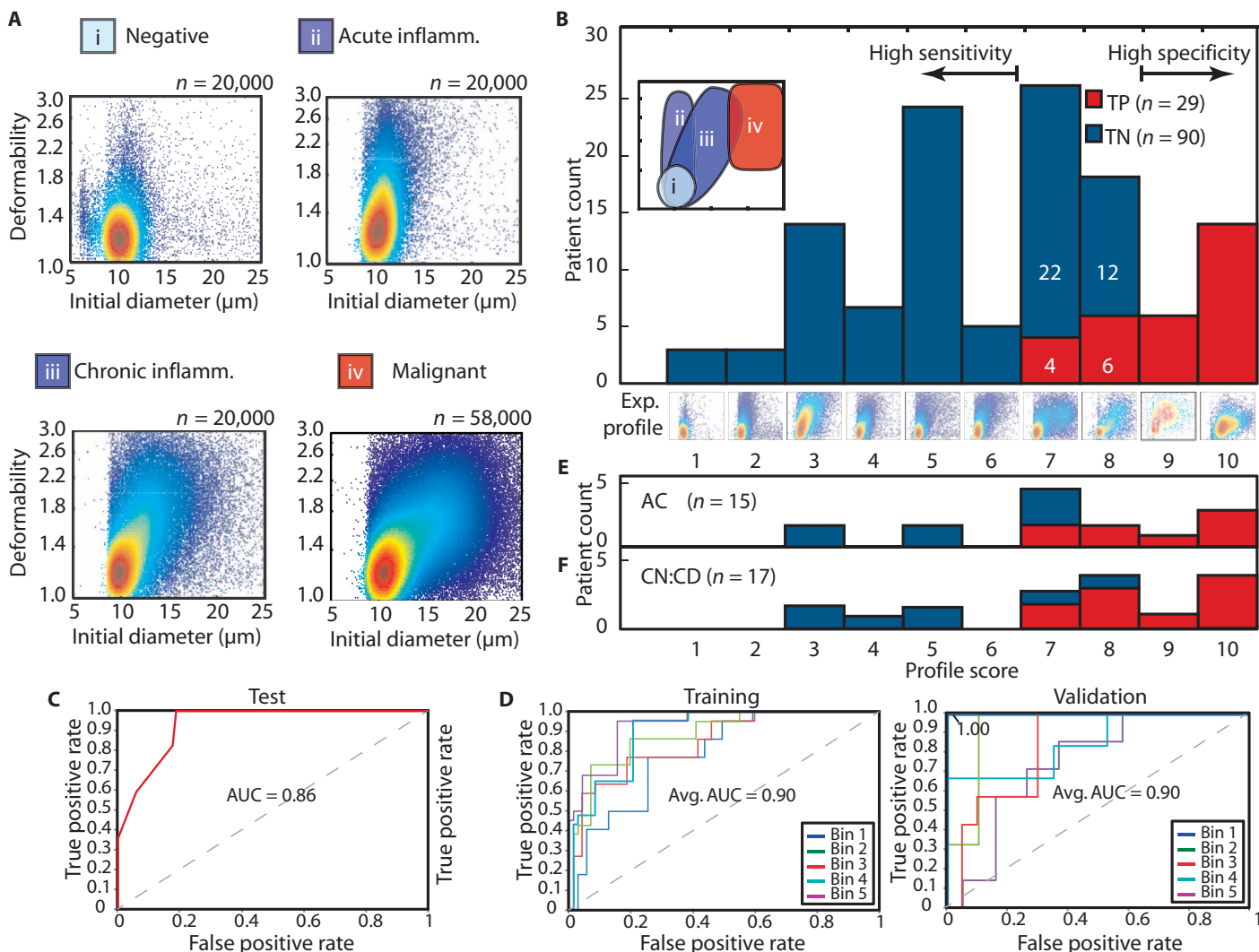


Fig. 3. Performance of scoring method using DC profile features.

(A) Pooled profiles of NMC, AI, CMI, and malignant outcomes. N is the number of single cells. (B) Distribution of DC profile scores versus clinical outcome of malignancy, where n is the number of patient samples that are true positive (TP) or true negative (TN). Inset graph shows regions of the 2D DC profile associated with different outcomes. (C) Receiver

operating characteristics (ROCs) for using threshold and weights identified in Table 1. (D) ROC for K -fold cross-validation of feature scoring method ($K = 5$). Cross-validation with five bins showing ROCs for the training and validation subsets. (E and F) DC profile scores and final outcomes for the subsets: ACs (E) and cytology-negative diagnosis but with concurrent disease (CN:CD) (F).

CMI-like features overlapping with moderate proportions of large and highly deformable malignant cells. Hence, 22.7% of samples with these scores were malignant samples, representing 34.5% of all malignant biopsies assayed.

By systematically changing the cutoff to classify a benign sample as malignant (from 1 to 10), we obtained varying sensitivity and specificity and generated an ROC, yielding an area under the curve (AUC) of 0.86 (Fig. 3C). Understanding that the thresholds and weights could be biased by defining the training and test sets in this manner, we performed a K -fold cross-validation (resampling method) to generate randomized test and validation subsets. Overall, validation of a K -fold ($K = 5$) population subset produced an average AUC of 0.90 (Fig. 3D). The scores reported throughout the main text made use of feature

thresholds and weights from the training set that yielded the highest performing validation subset (AUC 1.00) (Fig. 3D, bin 1). These thresholds and weights are provided in Table 1.

Separately, we performed independent analysis by machine-learning (ML) classifiers including logistic regression (fig. S2A), linear discriminant analysis (fig. S2B), and support vector machines (SVMs) based on summary statistics (means and SDs) (fig. S2, C to E) with fivefold cross-validation. These methods did not have access to the hand-engineered features discussed previously and so provided an indication of the generalizable signal present in the samples. The highest average AUC (0.79) was achieved using an SVM classifier with a quadratic kernel (fig. S2E). This indicates that the 11 selected profile features provide additional value over summary statistics in improving classification.

Table 1. List of the 11 extracted profile features used in the scoring algorithm. The threshold and weights used for the scores in the study are shown along with the threshold ranges and weighting ranges

extracted from the fivefold cross-validation test. Positive weights were connected to higher likelihood of malignancy, whereas negative weights led to a reduced likelihood.

Feature name	Feature description (type of identifier)	Threshold (range)	Weight (range)
1. Upper right quadrant limit 1	Threshold fraction of cells $d > 17 \mu\text{m}$ and $D > 1.4$ (MPE suspicion identifier)	>0.13 (0.05–0.08)	2 (1–2)
2. Upper right quadrant limit 2	Threshold fraction of cells $d > 17 \mu\text{m}$ and $D > 1.4$ (NMC identifier)	<0.06 (0.02–0.12)	–1 (–2 to –1)
3. Lower left quadrant limit	Threshold fraction of cells $d < 12 \mu\text{m}$ and $D < 1.4$ (NMC identifier)	>0.70 (0.65–0.70)	–3 (–4 to –3)
4. Deformability RMSE versus size-binned CMI standard	Absolute deformability RMSE between sample and CMI standard curve with 1- μm size bins (MPE suspicion identifier)	>0.12 (0.11–0.14)	1 (1–3)
5. Size RMSE versus deformability-binned CMI standard	Absolute size RMSE between sample and CMI standard curve with deformability bins of width = 0.5 (CMI identifier)	<0.50 (0.50–0.60)	–3 (–8 to –1)
6. Frequency RMSE versus size-binned CMI standard	Absolute frequency RMSE between sample and CMI standard curve with 1- μm size bins (CMI identifier)	<0.02 (0.01–0.03)	–3 (–3 to –1)
7. Deformability RMSE versus size-binned AI standard	Absolute deformability RMSE between sample and AI standard curve with 1- μm size bins (AI identifier)	<0.45 (0.05–0.45)	–2 (–3 to –1)
8. Size RMSE versus deformability-binned AI standard	Absolute size RMSE between sample and AI standard curve with deformability bins of width = 0.5 (AI identifier)	<0.06 (0.02–0.05)	–1 (–3 to –1)
9. Frequency RMSE versus size-binned AI standard	Absolute frequency RMSE between sample and AI standard curve with 1- μm size bins (AI identifier)	<0.06 (0.06–0.10)	–1 (–2 to –1)
10. Total RMSE	Sums AI and CMI RMSE to identify NMC that do not fit AI or CMI profiles (MPE suspicion identifier)	>0.40 (0.35–0.70)	2 (2–3)
11. Frequency RMSE versus size-binned NMC standard	Absolute frequency RMSE between sample and NMC standard curve based on frequency on the size axis (MPE suspicion identifier)	>0.13 (0.12–0.20)	2 (1–2)

Biophysical profiles associated with AC specimens

Morphological ambiguity within cell smears and blocks can lead to a cytological diagnosis of “atypical cells,” which necessitates one or more adjunct follow-up processes, such as flow cytometry, immunohistochemistry, fluorescence in situ hybridization (FISH), or invasive follow-up biopsies, to reach a conclusive finding. We asked the question of whether these cases also corresponded to samples in which DC gave equivocal scores (7 or 8), or whether they did not overlap and could provide additional information. Using DC, 53% of $n = 15$ atypical cases instead had profile scores with 100% predictive value (Fig. 3E). This is likely due to uniform population-level DC profile features for activated (reactive) leukocytes (Fig. 4, patients 23 to 25) and benign (reactive) mesothelial cells (Fig. 4, patients 21 and 22), because both cell populations can be cytomorphologically ambiguous compared to malignant cells (Fig. 4, patients 26 to 30).

Biophysical profiles of patients with concurrent disease specimens

Owing to the variable sensitivity of cytology alone, we defined the gold standard for a malignant outcome as the presence of disseminated disease, noted in the medical record within 6 months of the effusion. DC scores were also predictive of these late-stage malignancies that were cytology-negative but with concurrent disease (CN:CD) (Fig. 3F). Here, we looked at a subset of patients with concurrent disease (primary tumor or malignancies) ($n = 17$), identified retroactively as having a malignancy at the time of sample collection or within the 6 months after

sample collection. In this set of samples, true negatives corresponded to cases where the patient had either local lesions (nonleukemic) or ongoing chemotherapy treatments at the time of collection, where the patient did not have measurable disease within 6 months after thoracentesis. Notably, effusions from 5 of 10 patients with high-grade cancers that were cytology-negative scored in regions with high PPV for malignancy, and 5 of 7 patients with low-grade tumors (not metastasized) had scores of 6 or less (high NPV) (Fig. 3F). These data suggest that DC is predictive of malignancy and provides complementary information to traditional cytological analysis.

DISCUSSION

Thoracentesis procedures are performed at a rate of greater than 1.5 million per year in the United States (22). Malignant pleural fluids are drained to relieve patients of discomfort and also have clinical value in deducing etiology, diagnosing progression of malignant diseases, and monitoring patient relapse. Conventionally, pleural fluid samples are analyzed by cytology with adjunct procedures including flow cytometry, immunohistochemistry, and further biopsies, as required to reach a diagnosis. The burden of follow-up procedures and biopsies is a significant cost to the healthcare system. An accurate, low-cost, automated adjunct technique that limits the number of suspicious samples, which require focused follow-up, has the potential to reduce healthcare costs while providing better patient care.

Patients with inflammatory processes often yield suspicious samples that require additional time and analysis procedures to rule out malignancy. In AI, the response to infections is characterized by activation of the neutrophil population. Activated neutrophils are known to undergo physical changes as a result of extracellular stimuli resulting in more open chromatin and disintegration of the nuclear membrane (23–26). Cells undergoing these changes resemble hematological malignancies (27), making it difficult to reach a diagnosis based on conventional cell smears and cell blocks alone. Thus, specific immunolabels are often needed to confirm diagnoses using conventional methods. In CMI, mononuclear cells such as lymphocytes and macrophages are often the main cellular constituent of the effusion. Activated lymphocytes are identified by observation of increased size, globular nuclei, and other morphological changes (28). However, as with AI cases, conventional cell smears and cell blocks are often insufficient for ruling out malignancy owing to the CMI background, and these cases frequently require adjunct procedures to confirm diagnoses. Here, DC was able to classify 28 of 57 inflammation samples without concurrent malignant

cells with 100% NPV, suggesting the ability to avoid detailed follow-up in these cases.

DC could be implemented in the clinical workflow as an adjunct to traditional cytology or as a prescreening tool for identification of samples requiring the most detailed analysis. Implementing DC as an adjunct to cytological analysis can reduce cytology and follow-up workload. For example, the cytopathologist could make use of scores with high NPV (that is, scores ≤ 6) in a prescreening role and reduce analysis time spent on these samples. Overall, here, 56 samples fell within this high negative likelihood regime. Used in this manner, DC would have reduced the workload of cytological analysis by 47.1% (56 of 119). Furthermore, within this group of 56 negative samples, 25 follow-up requests that were ordered could have potentially been eliminated, reducing the total number of follow-up procedures by 45.5% (25 of 55 total requests from 119 patients).

Similarly, 19 of 29 MPE cases could have been rapidly identified because their scores of ≥ 9 indicated high likelihood of malignancy, thus eliminating an additional 12 follow-up requests. In summary, the total sample load for this study was 174 procedures (119 cell smear/block slide reads and an additional 55 follow-up analyses). Using DC in this manner, this load could be reduced by 112 analyses, or 64.3%: 56 high NPV samples, 25 high NPV follow-up procedures forgone, 19 high PPV samples, and 12 high PPV follow-ups forgone. Effusions with scores in an intermediate range would still be recommended for more detailed cytological analysis. In addition to the prescreening role, the DC score or the mechanophenotype profile may be used in adjunct with a cytology smear/block to improve overall diagnostic accuracy. This potential application, however, was not studied here.

The advantages of DC as a screening tool can be expected to have even greater impact in hospitals with limited resources or in developing economies with a lack of trained cytopathologists. Images from a smaller subset of the most suspicious samples (scores of 7 and 8) can be consulted out for telepathology. There are also advantages over conventional slide analysis with regard to archiving patient data. Currently, slides are rarely imaged and digitally archived because of the large memory requirements for storing image data, whereas DC profiles are discrete representations of patient data in an interpretable, information-rich, compact format that may be easily stored.

Nevertheless, there are limitations with our pilot study that require additional research to overcome. First, for malignant samples, it is often important to determine the cancer origin; however, with our current sample size, only a few samples from each cancer type were available, and it is unclear if we can distinguish between types of malignancy. Larger clinical studies will be necessary to determine whether DC can subclassify by cancer type. In addition, our current system is not completely automated, requiring an off-chip red blood cell lysis step, which should be avoided to reduce human intervention and variability.

These caveats in mind, combined with established label-based methods, label-free DC has the potential to improve the speed and accuracy of cancer diagnosis while simultaneously reducing costs to the health-care system. Still, further work is needed before the technology and results of this study can impact patient care, including commercial instrument and cartridge development with integrated red blood cell lysis, followed by larger clinical studies to develop training and validation sets that cover a broader range of cancer types with larger sample size for, especially, rare cancers. Following these advances, initial use in a prescreening role in cost-sensitive environments, such as managed or universal care, could spur adoption with simultaneous improvements in diagnostic accuracy of

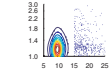
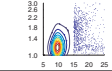
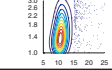
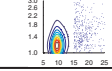
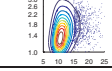
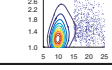
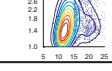
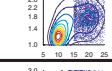
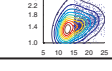
Pt. #	Cytology notes	Clinical outcome	DC analysis	
			Def. Size	Score
21	Mesothelial cells, reactive changes	NMC, RM		3
22	Mesothelial cells, reactive changes	NMC, RM		3
23	Reactive leukocytes	NMC		5
24	Reactive leukocytes	NMC, RM		5
25	Reactive leukocytes	NMC		7
26	Atypia	MPE, RM		8
27	Mesothelial cells, reactive changes	MPE, RM		9
28	Atypia	MPE, RM		10
29	Atypia	MPE		10
30	Mesothelial cells, reactive changes	MPE, RM		10

Fig. 4. DC profiles for pleural effusions that were diagnosed by cytology as containing ACs. Initial cytology readings were inconclusive, noting mesothelial reactive changes, reactive leukocytes, or atypia of cells. To achieve a final clinical outcome, adjunct follow-up procedures including flow cytometry, immunohistochemistry, FISH, and biopsies are typically used. The DC profile scores obtained in parallel to these adjunct procedures were predictive of the final clinical outcome.

malignancy. The DC platform should have broad use in many areas of biomedicine beyond cancer diagnostics, including immunology, regenerative medicine therapy, and drug-screening applications, where changes in cell state are accompanied by biophysical changes in cellular architecture.

MATERIALS AND METHODS

Study design

This pilot study tested the ability to quantitatively score malignant and NMC pleural effusions using DC with values correlated to 6-month patient outcomes obtained from the medical record for potential metastatic disease. All samples within a 24-hour cutoff from collection were included in the study. Patient samples were initially collected from the University of California, Los Angeles (UCLA) Cytopathology Lab, having arrived from clinics including UCLA Ronald Reagan Medical Center, UCLA Santa Monica Medical Center, and other regional hospitals over an 18-month period. Samples provided by cytopathology were remnants from thoracentesis after cytological examination and usually consisted of 10 to 50 ml of cellular fluid. For each sample, cell blocks and cell smears were prepared by conventional methods for cytomorphological analysis. Samples were received for biophysical analysis without receiving results of these conventional methods (that is, the clinical outcome was blinded to the operator). Subsequently, outcomes were later connected to the collected data without knowledge of the DC score. The design of both threshold classifier and support vector classifier was performed in a supervised fashion to arrive at the DC score.

One hundred nineteen patient samples were analyzed, in which a single sample was collected per patient and processed to obtain two to three videos. Quality control on collected videos included focal plane matching, cellularity checks, and cell velocity checks. We omitted from the analysis six consecutive malignant samples collected over a 5-week span owing to specimen preparation error. We suspect that this was due to sedimentation because larger cells were not observed in high frequency in any of the confirmed malignant samples, differing from the cytology cell smears. Additionally, 28 samples beyond a 24-hour cutoff were omitted owing to sample degradation (fig. S3A). Sample storage at room temperature or under 4°C refrigeration did not have an effect on median cell deformability (fig. S3B).

Microfluidic device fabrication and device dimensions

Microfluidic devices were designed in AutoCAD (Autodesk) and printed to transparency photomasks (CAD/Art Services Inc.). Transferring the designs on the photomasks to a replica mold was conducted by spinning negative photoresist, SU-8 50 (MicroChem), on a 4-inch silicon wafer at 4000 rpm. The coated wafer was soft baked at 65°C for 5 min and then at 95°C for 15 min. The wafer was then exposed under near ultraviolet at 8.0 mW/cm² for 30 s. A post-exposure bake of the wafer was carried out at 65°C for 2 min and then at 95°C for 3.5 min. The unexposed photoresist was developed in SU-8 Developer (MicroChem) until an isopropyl alcohol rinse produced no white film. The height of the resulting features was characterized by a surface profiler. The height and width immediately before the extensional flow junction were 28 and 67 μm, respectively. Devices were then cast with Sylgard 184 Silicone Elastomer (Dow Corning), PDMS, mixed 10 parts base to 1 part curing agent. The poured mold was degassed for 30 min followed by a

3-hour curing at 65°C. Devices were then cut from the mold, input and output ports were punched, and air plasma was cleaned for 30 s and bonded to plasma-activated glass slides. Devices were then placed in the 65°C oven for 3 hours before use.

Device operation

To prepare samples for DC mechanical phenotyping, they were first processed to remove red blood cells and debris by a hypotonic lysis buffer (Hoffman-La Roche). The samples were resuspended in a phosphate-buffered saline buffer (requiring 10 min of sample preparation time). At the optimal cell density between 200,000 and 300,000 cells/ml, cell-to-cell collision events in the junction are minimized. The suspensions were loaded into 3-ml plastic syringes (Becton Dickinson), connected with a 25-gauge luer stub (Instech Laboratories Inc.), and terminated with a short length of PEEK tubing (Upchurch Scientific) with an inner diameter of 0.02 inches and an outer diameter of 0.0313 inches. Equal tubing lengths were inserted into the outlets with free ends directed into a waste receptacle. The syringe was loaded onto a PHD 2000 syringe pump (Harvard Apparatus) and set to inject at a flow rate optimized for the device. A volumetric flow rate of 900 μl/min was optimal for prepared pleural fluid samples. At this flow rate, cells had more uniform trajectories when stretching in the extensional flow junction, in which we observe a steady but complex flow (fig. S4) (29). At the start of each run, devices were primed for 20 s with the same cell solution at the operational flow rate to allow for the flow rate to ramp to the set value considering the fluidic capacitance in the system. A 1.1-s video was then recorded, checked for quality, and downloaded to the computer (~30 s).

Data acquisition and processing

Video data were captured with a Vision Research Phantom v7.3 high-speed camera at 140,000 frames per second, with a 1-μs exposure. Videos were contrast-enhanced as part of the automated image analysis program. The automated image analysis code was built with MATLAB v2009a (MathWorks), and videos were processed on the UCLA Hoffman 2 Cluster. We have previously described the image analysis process (21) and graphics processing unit–based acceleration of image analysis algorithms (30). Briefly, for each cell, the predeformation size was extracted upon reaching the interrogation junction, and the maximum aspect ratio was extracted as the deformability, *D* (Fig. 1). Diameters of the cell are extracted by a polar to Cartesian coordinate transformation, where major and minor axes of the cells are extracted at 90 ± 30° and 0 ± 30°, respectively. The deformability parameter reported here is defined as the maximum ratio of major to minor axis calculated over all the frames in which the cell occupies the junction. Postprocessing scatter plots were created using dscatter function (creator: R. Henson, MathWorks File Exchange). Processing a video with 2000 cells required about 15 min to extract final DC plots and scores.

We targeted the collection of 3000 cell events per sample. Our analysis showed that the analysis of fewer than 1200 cells resulted in more variable scores that depended on which cells in the population were sampled (fig. S5). The variability in the mean and spread in SD was reduced for more than 1200 to 1500 cells per sample (P1 and P4). However, in some cases, such as samples P2 and P3, there was significant profile feature ambiguity such that scores fluctuated further, even up to 3000 cells in the sample, ultimately yielding equivocal seven and eight scores. Further increases in the number of cells analyzed per sample were limited by the memory size of the camera and additional

processing time, which can be overcome with hardware acceleration approaches (30).

Classification approach and design

The scoring algorithm is based on a linear combination of hand-crafted features, producing a linear decision boundary that is similar to those produced by logistic regression, SVMs, and other classification methods, including linear discriminant analysis. Scores were assigned on the basis of thresholds that exceed conditions of normality (NMC, AI, and CMI), where the score sum is connected to diagnostic accuracy for positive (high score) or negative cases (low score) (fig. S1). First, a simple gating of the upper right quadrant was created using the 95% confidence interval of the mean on NMC cases (fig. S1A). Then, by using a pooled analysis for characterization and development of standards for NMC, AI, and CMI, we further improve on specificity. Ten patient samples, where 2000 cells were randomly chosen from each sample, were used to generate pooled profiles. Each pooled profile was then described algorithmically by binning size and deformability at 1- μm and 0.2D intervals, respectively. The calculated median parameter of deformability or size with respect to each bin used the inner 90th percentile to represent core profile characteristics (fig. S1B). Last, we used the 90th percentile distribution of frequency of events in both binned deformability and size metrics to further correlate to NMC, AI, and CMI outcomes (fig. S1C).

The scoring system was trained on these parameters on the basis of DC profile features to maximize sensitivity for malignant specimens. A table of profile features and computationally optimized thresholds and weights is found in Table 1. To test the generalization of this classification method, we used *K*-fold cross-validation. We trained the scoring system (optimized thresholds and weights) on four of five subsamples, and its performance was assessed on the unobserved fold. This process was repeated a total of five times, covering every permutation of the observed/unobserved folds.

Definition of profile features

As stated above, 11 profile features with quantitative thresholds were defined for this analysis. The descriptions of feature profiles are listed in Table 1. These values are derived from the optimization of the classifier by fivefold cross-validation, and the threshold ranges listed are the maximum and minimum values of the optimization process. If a feature threshold described a particular sample, the score for that sample changes proportionally to the defined weight. For example, the first two profile features were designed to account for the importance of the fraction of cells within the large and deformable (upper right) quadrant; these three profile features are then defined as the fraction of cells within the large ($>17\ \mu\text{m}$) and deformable ($D > 1.4$) quadrant, and a sample may receive an adjustment to its profile score if the proportion in the quadrant meets threshold criteria. Multiple conditions can be met. The condition of the third profile feature is met if the fraction of cells within the lower left quadrant exceeds 0.65 to 0.70. Profile features 4 to 9 were defined as RMSEs, calculated for comparisons to AI and CMI cases. Three types of RMSE classifiers were developed. In the first type, cells are binned according to size with 1- μm increments (in both the sample of interest and an aggregate of, for example, pooled CMI cases); then, the RMSE between the mean deformability in each bin in the sample and the aggregate is calculated. If the sample was different from the aggregate, the RMSE would have been large; that is, a standard curve was generated for a pooled disease

case, and the sample was compared to the standard. The second type of RMSE comparison is the same except bins of similar deformability and means of size are used. In the third type, the RMSE is calculated for the difference in the fraction of cells in each size bin. Profile feature 10 is the sum of these RMSEs. Profile feature 11 is similar to the third type of RMSE comparison, but between the sample and pooled NMC cases.

We also built a model based on the summary statistics of each sample using standard ML classifiers to identify the importance of spatial profile features used in the scoring system and independently validate our analysis. In the ML analysis, we studied the performance and robustness of classifiers using the pleural fluid data set with an emphasis on out-of-sample prediction and without access to hand-crafted features. The inputs for the ML algorithms were the summary statistics extracted from the population of patient cells. In this case, each patient was summarized by maximum likelihood estimates of the mean and variance of the Gaussian distributions of the deformability and size of the patient cells. This resulted in a 4D feature representation of the patients. Using the *K*-fold cross-validation method described above, we implemented five widely used ML algorithms: logistic regression, linear discriminant analysis, and three different SVMs. The SVMs considered used linear, quadratic, and radial basis function kernels. Generalization performance of these classifiers was assessed via the ROC, summarized by the AUC metric (fig. S2).

This data set can be found in the Supplementary Materials. The file (SummaryStatDataset.csv) is CSV comma-delimited format with headers in row 1, final clinical outcomes in column 11, and scores using thresholds and weights from Table 1 in column 12. Additionally, per-patient single-cell data sets are provided (SingleCellDataset.mat). See the Supplementary Materials for structure format. The data set is deidentified.

Summary statistics

Medians and standard interquartile deviations were used to summarize single-cell population data. Data were not normally distributed and often consisted of several subpopulations.

SUPPLEMENTARY MATERIALS

www.sciencetranslationalmedicine.org/cgi/content/full/5/212/212ra163/DC1

Fig. S1. Components of the profile scoring algorithm.

Fig. S2. ROCs of three ML classifiers using a *K*-fold cross-validation method ($K = 5$).

Fig. S3. Effect of time and temperature on DC measurements.

Fig. S4. Extensional flow characteristics and stability.

Fig. S5. Sample size effects on DC scores.

File SummaryStatDataset.csv (summary-level data used to assign profile scores)

File SingleCellDataset.mat (single-cell data for 119 patients for diameter and deformability measurements)

REFERENCES AND NOTES

1. M. E. Froudarakis, Diagnostic work-up of pleural effusions. *Respiration* **75**, 4–13 (2008).
2. S. A. Sahn, State of the art. The pleura. *Am. Rev. Respir. Dis.* **138**, 184–234 (1988).
3. C. W. M. Bedrossian, Diagnostic problems in serous effusions. *Diagn. Cytopathol.* **19**, 131–137 (1998).
4. R. W. Light, Diagnostic principles in pleural disease. *Eur. Respir. J.* **10**, 476–481 (1997).
5. S. A. Sahn, The value of pleural fluid analysis. *Am. J. Med. Sci.* **335**, 7–15 (2008).
6. D. Di Carlo, A mechanical biomarker of cell state in medicine. *J. Lab. Autom.* **17**, 32–42 (2012).

7. S. E. Cross, Y. S. Jin, J. Rao, J. K. Gimzewski, Nanomechanical analysis of cells from cancer patients. *Nat. Nanotechnol.* **2**, 780–783 (2007).
8. T. W. Remmerbach, F. Wottawah, J. Dietrich, B. Lincoln, C. Wittekind, J. Guck, Oral cancer diagnosis by mechanical phenotyping. *Cancer Res.* **69**, 1728–1732 (2009).
9. M. Lekka, P. Laidler, Applicability of AFM in cancer detection. *Nat. Nanotechnol.* **4**, 72 (2009).
10. M. J. Rosenbluth, W. A. Lam, D. A. Fletcher, Force microscopy of nonadherent cells: A comparison of leukemia cell deformability. *Biophys. J.* **90**, 2994–3003 (2006).
11. J. D. Pajerowski, K. N. Dahl, F. L. Zhong, P. J. Sammak, D. E. Discher, Physical plasticity of the nucleus in stem cell differentiation. *Proc. Natl. Acad. Sci. U.S.A.* **104**, 15619–15624 (2007).
12. R. M. Hochmuth, Micropipette aspiration of living cells. *J. Biomech.* **33**, 15–22 (2000).
13. M. J. Rosenbluth, W. A. Lam, D. A. Fletcher, Analyzing cell mechanics in hematologic diseases with microfluidic biophysical flow cytometry. *Lab Chip* **8**, 1062–1070 (2008).
14. H. Bow, I. V. Pivkin, M. Diez-Silva, S. J. Goldfless, M. Dao, J. C. Niles, S. Suresh, J. Han, A microfabricated deformability-based flow cytometer with application to malaria. *Lab Chip* **11**, 1065–1073 (2011).
15. J. Chen, Y. Zheng, Q. Tan, E. Shojaei-Baghini, Y. L. Zhang, J. Li, P. Prasad, L. You, X. Y. Wu, Y. Sun, Classification of cell types using a microfluidic device for mechanical and electrical measurement on single cells. *Lab Chip* **11**, 3174–3181 (2011).
16. M. Abkarian, M. Faivre, H. A. Stone, High-speed microfluidic differential manometer for cellular-scale hydrodynamics. *Proc. Natl. Acad. Sci. U.S.A.* **103**, 538–542 (2006).
17. Y. Katsumoto, K. Tatsumi, T. Doi, K. Nakabe, Electrical classification of single red blood cell deformability in high-shear microchannel flows. *Int. J. Heat Fluid Flow* **31**, 985–995 (2010).
18. S. Byun, S. Son, D. Amodei, N. Cermak, J. Shaw, J. H. Kang, V. C. Hecht, M. M. Winslow, T. Jacks, P. Mallick, S. R. Manalis, Characterizing deformability and surface friction of cancer cells. *Proc. Natl. Acad. Sci. U.S.A.* **110**, 7580–7585 (2013).
19. J. Guck, S. Schinkinger, B. Lincoln, F. Wottawah, S. Ebert, M. Romeyke, D. Lenz, H. M. Erickson, R. Ananthakrishnan, D. Mitchell, J. Käs, S. Ulvick, C. Bilby, Optical deformability as an inherent cell marker for testing malignant transformation and metastatic competence. *Biophys. J.* **88**, 3689–3698 (2005).
20. A. M. Forsyth, J. Wan, W. D. Ristenpart, H. A. Stone, The dynamic behavior of chemically “stiffened” red blood cells in microchannel flows. *Microvasc. Res.* **80**, 37–43 (2010).
21. D. R. Gossett, H. T. K. Tse, S. A. Lee, Y. Ying, A. G. Lindgren, O. O. Yang, J. Rao, A. T. Clark, D. Di Carlo, Hydrodynamic stretching of single cells for large population mechanical phenotyping. *Proc. Natl. Acad. Sci. U.S.A.* **109**, 7630–7635 (2012).
22. R. W. Light, *Pleural Diseases* (Lippincott Williams & Wilkins, Philadelphia, PA, 2007).
23. S. Dharmawardhane, D. Brownson, M. Lennartz, G. M. Bokoch, Localization of p21-activated kinase 1 (PAK1) to pseudopodia, membrane ruffles, and phagocytic cups in activated human neutrophils. *J. Leukoc. Biol.* **66**, 521–527 (1999).
24. C. Knall, G. S. Worthen, G. L. Johnson, Interleukin 8-stimulated phosphatidylinositol-3-kinase activity regulates the migration of human neutrophils independent of extracellular signal-regulated kinase and p38 mitogen-activated protein kinases. *Proc. Natl. Acad. Sci. U.S.A.* **94**, 3052–3057 (1997).
25. V. Brinkmann, A. Zychlinsky, Neutrophil extracellular traps: Is immunity the second function of chromatin? *J. Cell Biol.* **198**, 773–783 (2012).
26. V. Brinkmann, A. Zychlinsky, Beneficial suicide: Why neutrophils die to make NETs. *Nat. Rev. Microbiol.* **5**, 577–582 (2007).
27. T. I. George, Malignant or benign leukocytosis. *Hematology Am. Soc. Hematol. Educ. Program* **2012**, 475–484 (2012).
28. D. G. E. Petrzilka, D. H. E. Schroeder, Activation of human T-lymphocytes. A kinetic and stereological study. *Cell Tissue Res.* **201**, 101–127 (1979).
29. R. R. Lagnado, L. G. Leal, Visualization of three-dimensional flow in a four-roll mill. *Exp. Fluids* **9**, 25–32 (1990).
30. H. T. K. Tse, P. Meng, D. R. Gossett, A. Irturk, R. Kastner, D. Di Carlo, Strategies for implementing hardware-assisted high-throughput cellular image analysis. *J. Lab. Autom.* **16**, 422–430 (2011).

Acknowledgments: We thank S. O’Byrne, J. Yu-Sheng, M. Cutidioc, A. Zopfi-Conklin, C. Lampa, C. Johnson, and M. Levin of the UCLA Cytopathology Lab for collecting and preparing samples for this study. Additionally, we are grateful for the helpful discussions and research assistance by S. O’Byrne, E. Wang, A. M. Shah, and A. C. H. Lee. We also thank the UCLA Academic Technology Services High Performance Computing group for providing computation services and P. Korambath for technical assistance. **Funding:** Supported by the David and Lucile Packard Foundation Fellowship in Science and Engineering (D.D.C.), an NSF Faculty Early Career Development Award (D.D.C.), and a Defense Advanced Research Projects Agency Young Faculty Award (D.D.C.). **Author contributions:** H.T.K.T., D.R.G., and D.D.C. designed the microfluidic device and DC approach; H.T.K.T., J.R., and D.D.C. designed the clinical study; Y.S.M. and R.P.A. designed and performed the ML analysis; H.T.K.T. and D.D.C. developed the scoring system; H.T.K.T. performed the scoring system analysis; Y.Y. and J.R. coordinated sample acquisition and transfer; H.T.K.T., D.R.G., and M.M. processed samples with DC; Y.Y. and K.M. extracted patient data; and H.T.K.T., D.R.G., M.S., Y.S.M., R.P.A., J.R., and D.D.C. wrote the paper. **Competing interests:** H.T.K.T. and D.R.G., at the submission of the paper, are employed at CytoVale Inc., which is commercializing the DC technology. The authors have equity interest in CytoVale Inc. **Data and materials availability:** The sample summary-level data and single-cell data from the study are available as part of the Supplementary Materials.

Submitted 13 May 2013

Accepted 28 October 2013

Published 20 November 2013

10.1126/scitranslmed.3006559

Citation: H. T. K. Tse, D. R. Gossett, Y. S. Moon, M. Masaeli, M. Sohsman, Y. Ying, K. Mislick, R. P. Adams, J. Rao, D. Di Carlo, Quantitative diagnosis of malignant pleural effusions by single-cell mechanophenotyping. *Sci. Transl. Med.* **5**, 212ra163 (2013).

Editor's Summary

Cytometry Device Helps (De)form a Diagnosis

Is it benign, or malignant? That is the main concern of cytopathologists as they screen cells in pleural effusions, taken from the lungs of patients suspected of having infections or cancer. This process is subjective and time-intensive and requires an expert's eye. So, to quickly "prescreen" samples for malignancy (and follow-up), Tse *et al.* describe deformability cytometry (DC)—an approach that relies on microfluidic forces to diagnose pleural effusion samples as malignant, or not.

The authors' device accelerates effusion samples through two opposing microfluidic channels. At the channels' four-way intersection, the cells are rapidly decelerated as they encounter the opposing flow, and then exit out the side channels. This leads to cell deformation, changing them from sphere-like shapes to pancakes. High-speed video of this intersection allowed Tse *et al.* to quantify cellular squishing: the more deformable the cell, the more malignant it is. The authors took 119 pleural effusion samples from patients with known clinical outcomes—negative for malignant cells (benign), acute inflammation, chronic/mixed inflammation, atypical cells, and malignant pleural effusions (MPEs)—to develop a diagnostic scoring system on a scale of 1 to 10, with 1 being benign. DC showed the best predictive abilities in two high-confidence regimes: 1 to 6 and 9 to 10. Scores of 7 and 8 were more difficult to diagnose, so these may be the types of samples where a cytopathologist's initial input would be necessary. Importantly, the authors looked at samples from patients that were cytology-negative with concurrent malignancy, such as a tumor, but 6 months later were diagnosed with disseminated disease. Five of 10 patients with high-grade cancers that were cytology-negative at sample collection scored high using DC. This suggests that the DC tool could be used to screen early for MPE.

Using deformability as a marker of disease will require additional validation in pleural effusion samples from patients with many different types of cancer. Nevertheless, owing to the ease of use and objective readout, with further clinical testing, DC should be useful as a quick screening tool to form an early diagnosis of MPEs.

A complete electronic version of this article and other services, including high-resolution figures, can be found at:

</content/5/212/212ra163.full.html>

Supplementary Material can be found in the online version of this article at:

</content/suppl/2013/11/18/5.212.212ra163.DC1.html>

Related Resources for this article can be found online at:

<http://stm.sciencemag.org/content/scitransmed/3/75/75ra26.full.html>

<http://stm.sciencemag.org/content/scitransmed/5/179/179ra47.full.html>

<http://stm.sciencemag.org/content/scitransmed/5/207/207ra142.full.html>

<http://stm.sciencemag.org/content/scitransmed/4/159/159ra147.full.html>

<http://stm.sciencemag.org/content/scitransmed/4/123/123ra26.full.html>

<http://stm.sciencemag.org/content/scitransmed/5/214/214ra170.full.html>

<http://www.sciencemag.org/content/sci/342/6163/1187.full.html>

<http://stm.sciencemag.org/content/scitransmed/6/219/219ra9.full.html>

<http://stm.sciencemag.org/content/scitransmed/6/261/261ra152.full.html>

<http://stm.sciencemag.org/content/scitransmed/6/267/267ra175.full.html>

Information about obtaining **reprints** of this article or about obtaining **permission to reproduce this article** in whole or in part can be found at:

<http://www.sciencemag.org/about/permissions.dtl>